

Light Field Synthesis by Training Deep Network in the Refocused Image Domain

Chang-Le Liu, Kuang-Tsu Shih, and Homer H. Chen, *Fellow, IEEE*

Abstract—Light field imaging, which captures spatio-angular information of incident light on image sensor, enables many interesting applications like image refocusing and augmented reality. However, due to the limited sensor resolution, a trade-off exists between the spatial and angular resolution. To increase the angular resolution, view synthesis techniques have been adopted to generate new views from existing views. However, traditional learning-based view synthesis mainly considers the image quality of each view of the light field and neglects the quality of the refocused images. In this paper, we propose a new loss function called refocused image error (RIE) to address the issue. The main idea is that the image quality of the synthesized light field should be optimized in the refocused image domain because it is where the light field is perceived. We analyze the behavior of RIL in the spectral domain and test the performance of our approach against previous approaches on both real and software-rendered light field datasets using objective assessment metrics such as MSE, MAE, PSNR, SSIM, and GMSD. Experimental results show that the light field generated by our method results in better refocused images than previous methods.

Index Terms—light field, view synthesis, CNN, image refocusing

I. INTRODUCTION

LIGHT field imaging enables users to refocus and change view-angle. A light field can be captured by a light field camera equipped with a microlens array [1], [2] or by a camera array [3]. The angular resolution of the light field captured by the former is limited by the number of pixels covered by microlens and the latter by the number of cameras. In practice, only limited angular resolution is available. To increase the angular resolution, view synthesis (interpolation) technique is often adopted to generate new views from the existing light field.

Some view synthesis methods first estimate the disparity map (or depth map) of the light field and use it to generate new views in between the existing views by warping the existing light field [4]–[7]. Recently, deep learning methods have also been developed for view synthesis of light field [8]–[10]. Such methods use several convolutional neural networks (CNN) to estimate the disparity map and refine the warped new views using an end-to-end training strategy. The output is a light field denser than the input light field. The loss functions used in these methods are mostly $L1$ or $L2$ metric. Furthermore, these metrics for evaluating the quality of the synthesized light field is

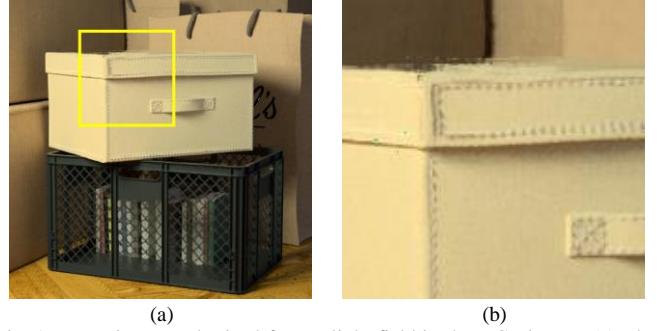


Fig. 1. New views synthesized from a light field in the HCI dataset. (a) The result generated by the network trained to minimize MAE. (b) is blowup view of (a). The network trained to minimize view-wise loss usually generates artifact at the region where occlusion occurs.

performed view-wise in the 4D light field domain. In our view, the quality of view synthesis for light field should be evaluated in the refocused image domain, because what matters ultimately is the perceived image, not the volume of 4D raw data.

To take the refocused image quality into consideration, we propose to add refocused image error (RIE) to the traditional view-wise loss function as a regularization term. RIL encourages the network to focus on the light field quality in the refocused image domain. It results in a dense light field, from which a better refocused image can be generated. An example improvement of our method is shown in Fig. 1.

The contributions of this paper can be summarized as follows:

- To our best knowledge, this is the first work that considers refocused image quality for light field synthesis and optimizes the deep network in the refocused image domain.
- We analyze the proposed refocused image error in the spectral domain and show the relation between evaluating $L2$ loss in 4D light field domain and that in the refocused image domain.
- We demonstrate that taking refocused image quality into consideration improves the performance of deep learning-based light field synthesis.

The rest of the paper is organized as follows. We review the related work in Section II and introduce the notation used in this paper in Section III. The proposed regularization and related analysis are described in Section IV. The experiment setting and the results are described in Section V. Finally, the concluding remarks are provided in Section VI.

II. RELATED WORK

A. Light Field Imaging

A light field [11] records the spatio-angular information of the light rays coming from different view angles. It contains angular information unavailable in the traditional 2D image data. Using the spatio-angular information, we may perform image refocusing to make any object in the scene in focus [1]. A light field can be captured by using an array of cameras [3] or a camera with a lenslet array [1]. The latter allows miniaturization of the device for consumer electronics [12], [13]. However, both types of light field cameras have limited angular resolution. The angular resolution of the former is limited by the number of cameras and the latter by the number of corresponding pixels of a lenslet.

B. View Synthesis for Light Field

View synthesis [3] has been developed to increase the angular resolution of a light field. Generally, view synthesis methods for the light field could be classified into two types.

The first type of methods [4], [5], [7] first estimate the depth information and then warp the existing views to generate new views by multi-view stereo algorithms [14], [15]. It is a depth-dependent process. The convolutional neural network (CNN) has also been adopted for view synthesis. Kalantari *et al.* proposed to use CNN to evaluate disparity information from the four corner views in an input light field. Another CNN was used to refine the new views generated the existing views and to estimate the depth map [9]. Srinivasan *et al.* extended this method to synthesize a light field only from the central view in the light field using an extra constraint on the consistency of ray depths [8].

The second type of methods synthesize a new image without depth information. This is made possible by limiting the configuration of input views to some specific patterns [16], [17]. Although the depth information is not required, the constraint on the configuration of input views limits the application of such methods. To overcome this problem and improve the performance for occlusion regions and non-Lambertian surfaces (which do not reflect light equally in all directions), for which depth-dependent methods often fail, Wang *et al.* proposed Pseudo 4DCNN [10] that adopts 3D CNN [18] to extract the 3D volume features by alternatively fixing an angular dimension of the input light field. That is, the Pseudo 4DCNN directly generate a dense light field by upsampling the input light field using deconvolution.

Although the above methods solve the light field view synthesis problem to a certain extent, the quality of refocused images is not explored. In this paper, we propose to add a regularization term called refocused image error to the loss function. It encourages the network to generate high-quality refocused images.

III. NOTATION

We consider the 4D light field proposed by Levoy and Hanrahan [3]. Denote a light field by $L(x, y, s, t)$, where the pairs (x, y) and (s, t) represent spatial and angular coordinates respectively. In practice, both s and t are finite; therefore, we

assume each of them is bounded by N . Because a 4D light field can be considered an image array captured from different viewpoints, we use $L_s(\mathbf{x})$, where $\mathbf{x} = (x, y)$, to denote the view captured at the angular coordinates $\mathbf{s} = (s, t)$. That is, $L_s(\mathbf{x})$ is a sub-aperture image at (s, t) .

The *shift-and-add* is the basic operation of image refocusing. In this operation, we first shift each sub-aperture image $L_s(\mathbf{x})$ by $\Delta \mathbf{x} = r\mathbf{s}$ and then average all shifted image to generate a refocused image R . More specifically,

$$R(L, r, \mathbf{x}) = \frac{1}{(2N+1)^2} \sum_{\mathbf{s}=(-N, -N)}^{(N, N)} L_s(\mathbf{x} + r\mathbf{s}). \quad (1)$$

Note that a larger r means refocusing farther from the camera and the sign of r decides the position of the refocused focal point with respect to the original focal point: positive means refocusing at a farther object and negative at a closer object.

In Section IV, we use \mathfrak{F} and \mathfrak{F}^{-1} to denote non-unitary Fourier transform and inverse Fourier transform. Note that we drop the constant coefficients like $1/2\pi$ in \mathfrak{F}^{-1} for simplicity, and this simplification does not affect our analysis. We use $\text{sinc}(x)$ to denote the unnormalized sinc function $\sin(x)/x$.

IV. REFOCUSED IMAGE ERROR

In this section, we first introduce the refocused image error and provide related analysis in the frequency domain.

A. Refocused Image Error

Assume there exists a desired light field L and a set of images S sampled from L . Given input S , we want to train a neural network G parameterized by θ to predict a light field $G_\theta(S)$ that is as similar as possible to L . Note that even though the input of the network is some views of the desired light field in this work, the proposed method has no restriction on the type of input. The only limitation is that the output must be a light field. Mathematically, the network G is trained to minimize the loss between $G_\theta(S)$ and L as follows:

$$\theta = \arg \min_{\theta} \mathcal{L}(G_\theta(S), L) \quad (2)$$

Traditionally, the loss function \mathcal{L} is chosen to be the mean-squared error (MSE) or the mean absolute error (MAE) between every image in L and $G_\theta(S)$. These view-wise MSE and view-wise MAE can be defined as follows:

$$\sum_{\mathbf{s}=(-N, -N)}^{(N, N)} \text{MAE}(L_s, G_\theta(S)_s) \quad (3)$$

$$\sum_{\mathbf{s}=(-N, -N)}^{(N, N)} \text{MSE}(L_s, G_\theta(S)_s) \quad (4)$$

This kind of loss functions only encourage the network to perform well on each sub-aperture image without considering the quality of refocused images generated from the predicted light field $G_\theta(S)$.

Instead, we propose the unweighted continuous refocused image error (UCRIE),

$$\begin{aligned} \text{UCRIE}_1(G_\theta(S), L) \\ = \frac{1}{2D} \int_{-D}^D \text{MAE}(R(G_\theta(S), r), R(L, r)) dr, \end{aligned} \quad (5)$$

$$\begin{aligned} \text{UCRIE}_2(G_\theta(S), L) \\ = \frac{1}{2D} \int_{-D}^D \text{MSE}(R(G_\theta(S), r), R(L, r)) dr, \end{aligned} \quad (6)$$

where D denotes the maximal value of r in the *shift-and-add* operation. Intuitively, UCRIE_2 and UCRIE_1 correspond to MSE and MAE, respectively. Also, it has been found empirically that the quality of a refocused image in (1) with r close to zero is more important for learning; therefore, we weight UCRIE by a Gaussian function $g(r) = \exp(-r^2)$ and define the continuous refocused image error (CRIE) as follows:

$$\begin{aligned} \text{CRIE}_1(G_\theta(S), L) \\ = \frac{1}{2D} \int_{-\infty}^{\infty} g(r) \text{MAE}(R(G_\theta(S), r), R(L, r)) dr, \end{aligned} \quad (7)$$

$$\begin{aligned} \text{CRIE}_2(G_\theta(S), L) \\ = \frac{1}{2D} \int_{-\infty}^{\infty} g(r) \text{MSE}(R(G_\theta(S), r), R(L, r)) dr. \end{aligned} \quad (8)$$

Note that the definite integral is replaced with improper integral in CRIE for simplification in the spectral domain. (By the definition of $g(r)$, this makes a trivial difference when D is larger than 3.) Incidentally, we adopt definite integral for UCRIE to prevent it from diverges when D goes to infinity. An analysis of CRIE in the spectral domain is given in Sec. IV.B to explain why we add $g(r)$.

Although r in UCRIE and CRIE can have infinitely many values, evaluating an equation on infinitely many points is difficult. In practice, the following losses, called refocused image errors (RIEs) in this work, are more appropriate for deep learning and quality evaluation tasks:

$$\begin{aligned} \text{RIE}_1(G_\theta(S), L) \\ = \frac{1}{2D} \sum_{r=-D}^D g(r) \text{MAE}(R(G_\theta(S), sr), R(L, sr)), \end{aligned} \quad (9)$$

$$\begin{aligned} \text{RIE}_2(G_\theta(S), L) \\ = \frac{1}{2D} \sum_{r=-D}^D g(r) \text{MSE}(R(G_\theta(S), sr), R(L, sr)), \end{aligned} \quad (10)$$

where s is the step interval of the summation.

B. Spectral Domain Analysis

Here we analyze the characteristics of CRIE in the spectral domain. First, we may rewrite CRIE_2 using Fourier transform and Plancherel's formula as follows:

$$\begin{aligned} \text{UCRIE}_2(G_\theta(S), L) = \\ \frac{1}{(2N+1)^4} \sum_{\mathbf{s}, \mathbf{t}} \sum_{\boldsymbol{\omega}} \mathcal{E}_{\mathbf{s}}(\boldsymbol{\omega}) \mathcal{E}_{\mathbf{t}}(\boldsymbol{\omega}) \text{sinc}(D\boldsymbol{\omega}^T(\mathbf{s}+\mathbf{t})), \end{aligned} \quad (11)$$

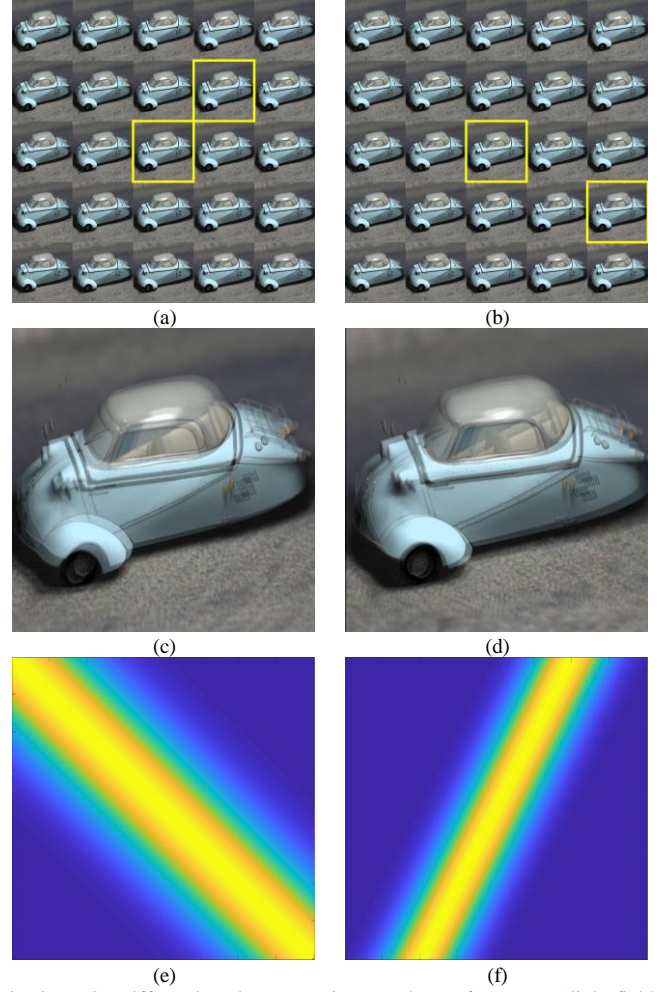


Fig. 2. (a)(b) Differently sub-aperture images chosen from a 5×5 light field. (c) and (d) are the superposition of two sub-aperture images correspond to (a) and (b). (e) is 135-degree orientated Gaussian function. (f) is 60-degree orientated Gaussian function.

where $\mathcal{E}_{\mathbf{s}} = \mathfrak{F}\{G_\theta(S)_{\mathbf{s}} - L_{\mathbf{s}}\}$ denotes the spectrum of the error of the sub-aperture image at \mathbf{s} . Similarly, CRIE_2 can be rewritten as

$$\begin{aligned} \text{CRIE}_2(G_\theta(S), L) = \\ \frac{1}{(2N+1)^4} \sum_{\mathbf{s}, \mathbf{t}} \sum_{\boldsymbol{\omega}} \mathcal{E}_{\mathbf{s}}(\boldsymbol{\omega}) \mathcal{E}_{\mathbf{t}}(\boldsymbol{\omega}) \frac{\sqrt{\pi}}{2D} e^{-0.25(\boldsymbol{\omega}^T(\mathbf{s}+\mathbf{t}))^2} \end{aligned} \quad (12)$$

The derivation of Eqs. (11) and (12) is given in Appendix.

Eqs. (11) and (12) suggest that the refocused continuous refocused image error measures the error filtered by a low-pass filter: sinc filter for UCRIE_2 and Gaussian filter for CRIE_2 . By the definition of MSE, we can also rewrite (3) in frequency domain as

$$\sum_{\mathbf{s}=(-N, -N)}^{(N, N)} \text{MSE}(L_{\mathbf{s}}, G_\theta(S)_{\mathbf{s}}) = \sum_{\forall \mathbf{s}, \mathbf{t}, \mathbf{s}=\mathbf{t}} \sum_{\boldsymbol{\omega}} \mathcal{E}_{\mathbf{s}}(\boldsymbol{\omega}) \mathcal{E}_{\mathbf{t}}(\boldsymbol{\omega}). \quad (13)$$

We can see that view-wise MSE is a simplification of Eq. (12). Compare both CRIE_2 and UCRIE_2 with traditional view-wise MSE, we can see there are two main differences. First the

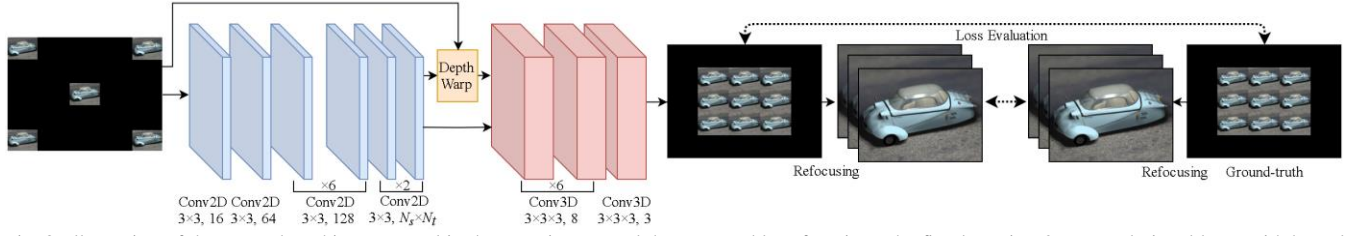


Fig. 3. Illustration of the network architecture used in the experiments and the proposed loss function. The first layer is a 2D convolutional layer with kernel size = 3×3 and channel number = 16. Other layers follow the same rule. N_s and N_t denote the number of views along the two axes.

traditional view-wise MSE does not consider the correlation between two different views captured from different view angles. Second, the errors measured by CRIE_2 and UCRIE_2 are filtered by a directional filter. That is, the weighting for each $\sum_{\omega} \mathcal{E}_s(\omega) \mathcal{E}_t(\omega)$ in Eqs. (11) and (12) depends on the vector value of $\mathbf{s} + \mathbf{t}$. Take CRIE_2 for example and let $\mathbf{s} = (0, 0)$ W.L.O.G. Assume $\mathbf{s} + \mathbf{t} = (1, 1)$. Then L_t is in the top right of L_s , as marked in the Fig. 2(a). According to Eq. (12), we see the weight of $\mathcal{E}_s(\omega) \mathcal{E}_t(\omega)$ is an 135-degree orientated low-pass Gaussian filter, as shown in Fig. 2(e). This is reasonable. If we *shift-and-add* L_s and L_t : L_t moves toward (away) from L_s when r is positive (negative) in the 45-degree orientation, we get an image with motion blur in the 45-degree orientation, as shown in Fig. 2(c). In other case, assume $\mathbf{s} + \mathbf{t} = (2, -1)$, as shown in Fig. 2(b). Then the weight is a 60-degree orientated low-pass Gaussian filter Fig. 2(f), and the superposition of L_s and L_t , as shown in Fig. 2(d).

The above analysis also explains why CRIE_2 is better than UCRIE_2 . The Gaussian filter is non-negative and non-oscillatory and hence causes no ringing effect in the spectral domain.

For CRIE_1 and UCRIE_1 , we can analyze them in a similar way. By using Chebyshev approximation [19] and omitting terms higher than the fourth order, we have the following:

$$\begin{aligned} \text{CRIE}_1(G_\theta(S), L) &= \frac{-1}{\pi} \frac{1}{2D} \left(\frac{1}{2N+1} \right)^2 \\ &\int_{-\infty}^{\infty} e^{-r^2} \left\{ \sum_x \left(\sum_{k=1}^{\infty} \frac{(-1)^k T_{2k}(\tau(x, r))}{-1 + 4k^2} \right) \right\} dr, \quad (14) \\ \tau(x, r) &= R(G_\theta(S), r) - R(L, r), \end{aligned}$$

where T_{2k} is a Chebyshev polynomial of the first kind. By expanding (14), we can find that CRIE_1 includes CRIE_2 .

V. EXPERIMENTS SETUP AND RESULTS

In this section, we first describe the network architecture used in our experiment for view synthesis and the experimental setup.

Then, we describe the results of our experiment for testing the performance of the proposed RIE for light field synthesis.

A. Network Architecture

The proposed RIE can be applied to a neural network trained through backpropagation for light field synthesis. We started with the deep neural network architecture proposed by Srinivasan1 *et al.* [8] for light field synthesis. In our opinion, synthesizing a light field from multiple views is more robust than from a single view, thus we fed a total of five views into the network as inputs. This architecture mainly consists of two sub-networks, both fully convolutional networks. The first sub-network estimated the depth map of each new view, based on which an approximate Lambertian light field was synthesized by warping the central view. The second sub-network predicted a residual light field to be added to the synthesized Lambertian light field and handled occluded parts and non-Lambertian effects [8]. The details of the network layers are shown in Fig. 3. In our experiment, we trained two networks to minimize the following two loss functions, one for each network:

$$\sum_{s=(-N, -N)}^{(N, N)} \text{MAE}(L_s, G_\theta(S)_s) + \lambda_R \text{RIE}_1(G_\theta(S), L), \quad (15)$$

$$\sum_{s=(-N, -N)}^{(N, N)} \text{MSE}(L_s, G_\theta(S)_s) + \lambda_R \text{RIE}_2(G_\theta(S), L), \quad (16)$$

where λ_R denotes the RIE regularization parameters. For comparison, we trained another two networks to minimize Eqs. (3) and (4).

Note that at first glance, Eqs. (11) and (12) may be used to evaluate Eqs. (7) and (8) on infinitely many samples of r . However, training the network using Eqs. (11) and (12) as the loss function is usually unstable. This is why Eqs. (9) and (10) are used in Eqs. (15) and (16) respectively for network training in our experiments.

B. Experimental Setup

We evaluated the network performance in terms of following standard objective metrics: MAE, MSE, the peak signal-to-noise ratio (PSNR), the gray-scale structural similarity (SSIM) [20], and the gradient magnitude similarity deviation (GMSD) [21]. GMSD is an image quality metric that uses the standard deviation of the pixel-wise gradient magnitude similarity (GMS) to evaluate image quality,

$$\text{GMS}(\mathbf{x}) = \frac{2m_r(\mathbf{x})m_d(\mathbf{x}) + c}{m_r^2(\mathbf{x}) + m_d^2(\mathbf{x}) + c}, \quad (17)$$

$$\text{GMSD} = \sqrt{\frac{1}{M} \sum_{\mathbf{x}} (\text{GMS}(\mathbf{x}) - \frac{1}{M} \sum_{\mathbf{x}} \text{GMS}(\mathbf{x}))^2},$$

where M is the number of pixels, m_r and m_d are gradient magnitudes of the reference and the distorted images, respectively. The worse the distorted image, the higher GMSD is.

We trained the networks on two light field datasets: the synthetic light fields (HCI dataset) [22] and the real light fields (INRIA dataset [23]). We partitioned the HCI dataset into sixteen light fields for training and eight for testing) and the INRIA dataset into 43 light fields for training and 16 for testing. Both HCI and INRIA datasets have a spatial resolution of 512×512 . But the former has angular resolution of 9×9 , and the latter 7×7 . Furthermore, we extracted sub-lightfields of 5×5 views from each dataset. A total of 25 sub-lightfields were extracted from the HCI dataset and nine from the INRIA dataset. For each sub-lightfield, we use the central view and the four corner views as input to the view synthesis network. The output is a 3×3 light field, as shown in Fig. 3.

For each new view, the corresponding view at the same position in the original light field was used as the ground-truth. For RIE evaluation, we set $D = 2.5$, $r = 0.25$ and $\lambda_R = 1$. All neural network models were trained with the Adam optimization algorithm [24] and default parameters $\beta_1 = 0.9$, $\beta_2 = 0.999$, $\epsilon = 1e-08$.

C. Experimental Results

We first evaluated the two networks (called $MSE+RIE_2$ and $MAE+RIE_1$) trained by optimizing the proposed loss functions and the other two (called MSE and MAE) trained by optimizing Eqs. (3) and (4). The MAE, MSE, PSNR, SSIM, and GMSD scores are listed in Table I and II. From the tables, we can see the PSNR and MSE scores of $MSE+RIE_2$ and $MAE+RIE_1$ are higher than those of MSE and MAE , respectively. In addition, $MAE+RIE_1$ and MAE are better than $MSE+RIE_2$ and MSE in terms of these metrics, which shows MAE is a better loss function compared with MSE for light field synthesis. The results are in line with the results got in the work of Zhao *et. al.* [25] for image restoration.

The blowup output images and corresponding ground-truth are shown in Fig. 4. Comparing with the results of MSE and MAE , we can see that the results of $MSE+RIE_2$ and $MAE+RIE_1$ are less noisy and more stable. From Fig. 4(b) and (c), we can see that compared with $MAE+RIE_1$, MAE produces artifacts at the region occlusion occurs.

resolution input wide-angle image, we can see that the sharpness is significantly enhanced.

In addition to evaluate the overall quality of 4D light field, we further evaluated the refocused images quality. The MAE, MSE, PSNR, SSIM, and GMSD scores of refocused images of the four networks with $r = 0$ are listed in Table III and IV. From Table III, we can see $MSE+RIE_2$ and $MAE+RIE_1$ performs better than MSE and MAE in terms of MAE, PSNR, and GMSD,

TABLE I
COMPARISON OF OUR APPROACH AGAINST TRADITIONAL LOSS FUNCTION IN TERMS OF 4D LIGHT FIELD ON HCI DATASET

Quality Assessment	Used loss function in training			
	MSE	$MSE+RIE_2$	MAE	$MAE+RIE_1$
MAE	0.0180	0.0176	0.0152	0.0156
MSE	0.0032	0.0029	0.0012	0.0010
PSNR	27.310	28.098	30.340	30.727

TABLE II
COMPARISON OF OUR APPROACH AGAINST TRADITIONAL LOSS FUNCTION IN TERMS OF 4D LIGHT FIELD ON INRIA DATASET

Quality Assessment	Used loss function in training			
	MSE	$MSE+RIE_2$	MAE	$MAE+RIE_1$
MAE	0.0176	0.0094	0.0091	0.0091
MSE	0.0030	0.0003	0.0005	0.0004
PSNR	27.805	36.397	33.354	35.213

TABLE III
COMPARISON OF OUR APPROACH AGAINST TRADITIONAL LOSS FUNCTION IN TERMS OF REFOCUSED IMAGES ON HCI DATASET

Quality Assessment	Used loss function in training			
	MSE	$MSE+RIE_2$	MAE	$MAE+RIE_1$
MAE	0.0096	0.0091	0.0071	0.0070
MSE	0.0008	0.0007	0.0002	0.0002
PSNR	31.087	31.283	37.183	38.308
SSIM	0.8243	0.8358	0.8468	0.8415
GMSD	0.0461	0.0371	0.0269	0.0240

TABLE IV
COMPARISON OF OUR APPROACH AGAINST TRADITIONAL LOSS FUNCTION IN TERMS OF A REFOCUSED IMAGES ON INRIA DATASET

Quality Assessment	Used loss function in training			
	MSE	$MSE+RIE_2$	MAE	$MAE+RIE_1$
MAE	0.0093	0.0043	0.0043	0.0041
MSE	7.08e-4	4.00e-5	6.82e-5	4.12e-5
PSNR	31.523	44.0113	41.7215	43.8753
SSIM	0.8271	0.9129	0.9143	0.9163
GMSD	0.0428	0.0055	0.0132	0.0074

but on INRIA dataset, the former two outperforms the latter two in terms of all five metrics.

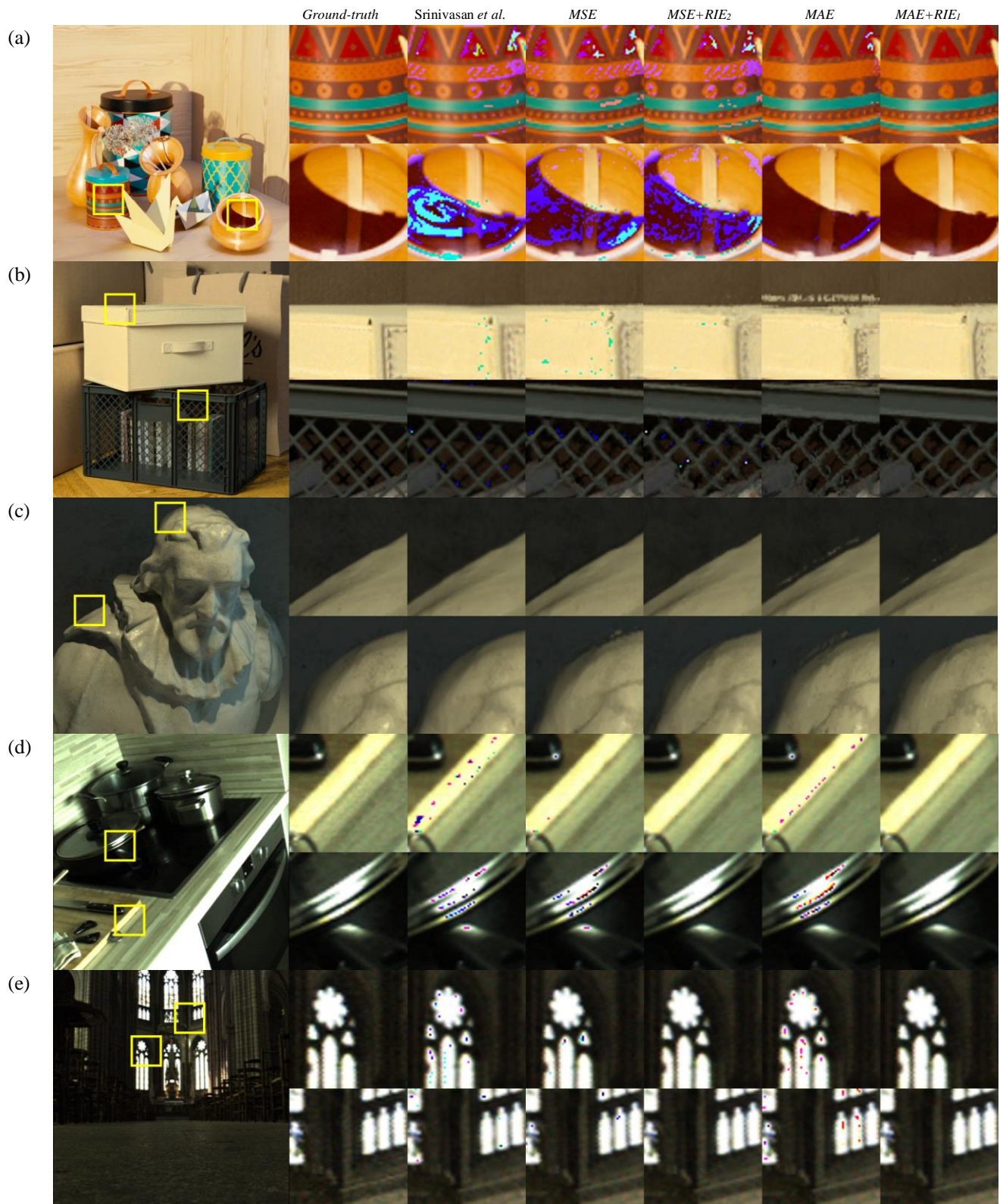
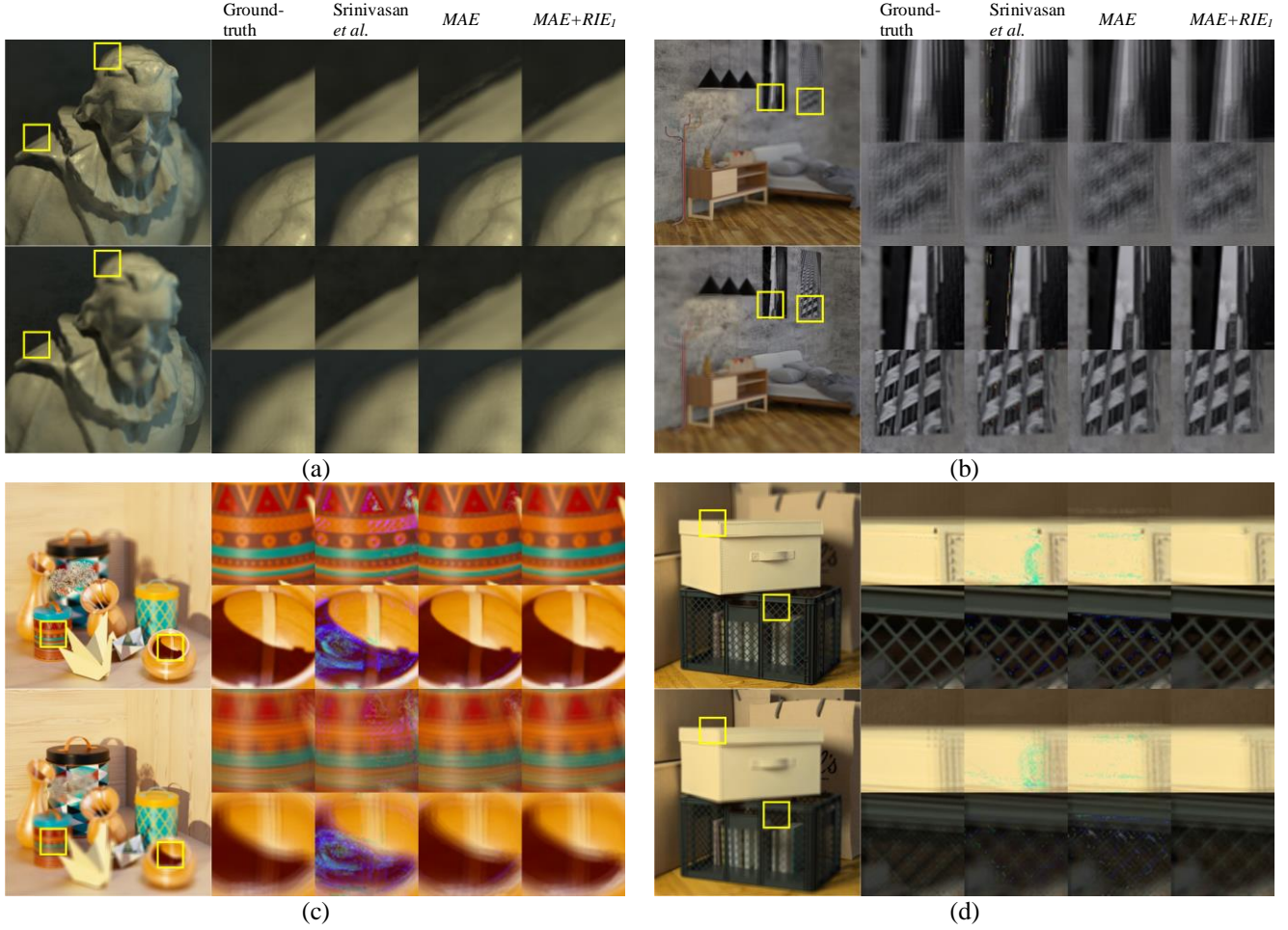


Fig. 4. Experimental results on HCI and INRIA datasets. We show ground-truth image and the close-ups generated

VI. CONCLUSION

In this paper, we have proposed a novel regularization called refocused image error for light field synthesis that encourages

the deep network to generate high-quality refocused images. In our design, a deep network is optimized to minimize light field loss in the 4D light field domain and refocused image domain at the same time. We have also analyzed our refocused image error in the spectral domain and verified the relation between



refocused images and the raw light field. Experiments on real and software-rendered light field datasets have shown the effectiveness of the proposed regularization.

APPENDIX

For simplicity, \hat{L} denotes the alias of $G_\theta(S)$ and $L_s^h = L_s(\mathbf{x} + \mathbf{h})$.

$$\begin{aligned}
 & \text{UCRIE}_2(\hat{L}, L) \\
 &= \frac{1}{2D} \int_{-D}^D \text{MSE}(R(\hat{L}, r), R(L, r)) dr \\
 &= \frac{1}{2D} \int_{-D}^D \sum_{\mathbf{x}} (R(\hat{L}, r, \mathbf{x}) - R(L, r, \mathbf{x}))^2 dr \\
 &= \frac{1}{2D} \int_{-D}^D \sum_{\mathbf{x}} \left(\frac{1}{(2N+1)^2} \sum_s \hat{L}_s^r(\mathbf{x} + r\mathbf{s}) - \frac{1}{(2N+1)^2} \sum_s L_s^r(\mathbf{x} + r\mathbf{s}) \right)^2 dr \\
 &= \frac{1}{2D(2N+1)^4} \int_{-D}^D \sum_{\mathbf{x}} \left(\sum_s (\hat{L}_s^r(\mathbf{x}) - L_s^r(\mathbf{x}))^2 \right) dr \\
 &= \frac{1}{2D(2N+1)^4} \int_{-D}^D \sum_{s,t} \sum_{\mathbf{x}} (\hat{L}_s^r(\mathbf{x}) - L_s^r(\mathbf{x})) (\hat{L}_t^r(\mathbf{x}) - L_t^r(\mathbf{x})) dr
 \end{aligned}$$

For simplicity, let $\mathcal{E}_s = \mathfrak{F}\{\hat{L}_s - L_s\}$. Then, by Plancherel's formula and the translation property of Fourier transform:

$$\begin{aligned}
 & \frac{1}{2D(2N+1)^4} \int_{-D}^D \sum_{s,t} \sum_{\mathbf{x}} (\hat{L}_s^r(\mathbf{x}) - L_s^r(\mathbf{x})) (\hat{L}_t^r(\mathbf{x}) - L_t^r(\mathbf{x})) dr \\
 &= \frac{1}{2D(2N+1)^4} \int_{-D}^D \sum_{s,t} \sum_{\omega} (\mathcal{E}_s(\omega) e^{jr\omega^T \mathbf{s}}) (\mathcal{E}_t(\omega) e^{jr\omega^T \mathbf{t}}) dr \\
 &= \frac{1}{(2N+1)^4} \sum_{s,t} \sum_{\omega} \mathcal{E}_s(\omega) \mathcal{E}_t(\omega) \frac{1}{2D} \int_{-D}^D e^{jr\omega^T (\mathbf{s} + \mathbf{t})} dr \\
 &= \frac{1}{(2N+1)^4} \sum_{s,t} \sum_{\omega} \mathcal{E}_s(\omega) \mathcal{E}_t(\omega) \text{sinc}(D\omega^T (\mathbf{s} + \mathbf{t}))
 \end{aligned}$$

The proof is completed. For CRIE, we only need to replace D with infinity and add $g(r)$ to the equation:

$$\begin{aligned}
 & \text{CRIE}_2(G_\theta(S), L) = \\
 & \left(\frac{1}{2N+1} \right)^4 \sum_{s,t} \sum_{\omega} \mathcal{E}_s(\omega) \mathcal{E}_t(\omega) \frac{1}{2D} \int_{-\infty}^{\infty} e^{-r^2} e^{jr\omega^T (\mathbf{s} + \mathbf{t})} dr \\
 &= \frac{1}{(2N+1)^4} \sum_{s,t} \sum_{\omega} \mathcal{E}_s(\omega) \mathcal{E}_t(\omega) \frac{\sqrt{\pi}}{2D} e^{-0.25(\omega^T (\mathbf{s} + \mathbf{t}))^2}
 \end{aligned}$$

This completes the proof.

References

- [1] R. Ng *et al.*, “Light Field Photography with a Hand-held Plenoptic Camera,” p. 11.
- [2] T. Georgeiv, K. C. Zheng, B. Curless, D. Salesin, S. Nayar, and C. Intwala, “Spatio-Angular Resolution Tradeoff in Integral Photography,” p. 10.
- [3] M. Levoy and P. Hanrahan, “Light field rendering,” in *Proceedings of the 23rd annual conference on Computer graphics and interactive techniques - SIGGRAPH '96*, Not Known, 1996, pp. 31–42.
- [4] G. Chaurasia, O. Sorkine, and G. Drettakis, “Silhouette-Aware Warping for Image-Based Rendering,” *Comput. Graph. Forum*, vol. 30, no. 4, pp. 1223–1232, Jun. 2011.
- [5] G. Chaurasia, S. Duchene, O. Sorkine-Hornung, and G. Drettakis, “Depth synthesis and local warps for plausible image-based navigation,” *ACM Trans. Graph.*, vol. 32, no. 3, pp. 1–12, Jun. 2013.
- [6] S. Wanner and B. Goldluecke, “Variational Light Field Analysis for Disparity Estimation and Super-Resolution,” *IEEE Trans. Pattern Anal. Mach. Intell.*, vol. 36, no. 3, pp. 606–619, Mar. 2014.
- [7] M. Goesele, J. Ackermann, S. Fuhrmann, C. Haubold, R. Klowinsky, and T. Darmstadt, “Ambient point clouds for view interpolation,” *ACM Trans. Graph.*, vol. 29, no. 4, p. 1, Jul. 2010.
- [8] P. P. Srinivasan, T. Wang, A. Sreelal, R. Ramamoorthi, and R. Ng, “Learning to Synthesize a 4D RGBD Light Field from a Single Image,” *ArXiv170803292 Cs*, Aug. 2017.
- [9] N. K. Kalantari, T.-C. Wang, and R. Ramamoorthi, “Learning-based view synthesis for light field cameras,” *ACM Trans. Graph.*, vol. 35, no. 6, pp. 1–10, Nov. 2016.
- [10] Y. Wang, F. Liu, Z. Wang, G. Hou, Z. Sun, and T. Tan, “End-to-End View Synthesis for Light Field Imaging with Pseudo 4DCNN,” in *Computer Vision – ECCV 2018*, vol. 11206, V. Ferrari, M. Hebert, C. Sminchisescu, and Y. Weiss, Eds. Cham: Springer International Publishing, 2018, pp. 340–355.
- [11] G. Lippmann, “La photographie integrale,” *ComptesRendus Acad. Sci.*, 1908.
- [12] “Lytro.” [Online]. Available: <https://www.lytro.com/>.
- [13] “Raytrix,” 2018. [Online]. Available: <https://raytrix.de/>.
- [14] M. Goesele, N. Snavely, B. Curless, H. Hoppe, and S. M. Seitz, “Multi-View Stereo for Community Photo Collections,” in *2007 IEEE 11th International Conference on Computer Vision*, Rio de Janeiro, Brazil, 2007, pp. 1–8.
- [15] Y. Furukawa and J. Ponce, “Accurate, Dense, and Robust Multi-View Stereopsis,” p. 8.
- [16] A. Levin and F. Durand, “Linear view synthesis using a dimensionality gap light field prior,” in *2010 IEEE Computer Society Conference on Computer Vision and Pattern Recognition*, 2010, pp. 1831–1838.
- [17] L. Shi, H. Hassanieh, A. Davis, D. Katabi, and F. Durand, “Light Field Reconstruction Using Sparsity in the Continuous Fourier Domain,” *ACM Trans. Graph.*, vol. 34, no. 1, pp. 1–13, Dec. 2014.
- [18] D. Tran, L. Bourdev, R. Fergus, L. Torresani, and M. Paluri, “Learning Spatiotemporal Features with 3D Convolutional Networks,” in *2015 IEEE International Conference on Computer Vision (ICCV)*, Santiago, Chile, 2015, pp. 4489–4497.
- [19] P. R. Clement, “The Chebyshev approximation method,” *Q. Appl. Math.*, vol. 11, no. 2, pp. 167–183, Jul. 1953.
- [20] Z. Wang, A. C. Bovik, H. R. Sheikh, and E. P. Simoncelli, “Image Quality Assessment: From Error Visibility to Structural Similarity,” *IEEE Trans. Image Process.*, vol. 13, no. 4, pp. 600–612, Apr. 2004.
- [21] W. Xue and L. Zhang, “Gradient Magnitude Similarity Deviation: An Highly Efficient Perceptual Image Quality Index,” p. 12.
- [22] K. Honauer, O. Johannsen, D. Kondermann, and B. Goldluecke, “A Dataset and Evaluation Methodology for Depth Estimation on 4D Light Fields,” in *Computer Vision – ACCV 2016*, vol. 10113, S.-H. Lai, V. Lepetit, K. Nishino, and Y. Sato, Eds. Cham: Springer International Publishing, 2017, pp. 19–34.
- [23] X. Jiang, M. Le Pendu, R. A. Farrugia, and C. Guillemot, “Light Field Compression With Homography-Based Low-Rank Approximation,” *IEEE J. Sel. Top. Signal Process.*, vol. 11, no. 7, pp. 1132–1145, Oct. 2017.
- [24] D. P. Kingma and J. Ba, “Adam: A Method for Stochastic Optimization,” *ArXiv14126980 Cs*, Dec. 2014.
- [25] H. Zhao, O. Gallo, I. Frosio, and J. Kautz, “Loss Functions for Image Restoration with Neural Networks,” *IEEE Trans. Comput. IMAGING*, vol. 3, no. 1, p. 11, 2017.